Applied Catalysis A: General 457 (2013) 12–20

Contents lists available at SciVerse ScienceDirect

Applied Catalysis A: General

journal homepage: www.elsevier.com/locate/apcata

One-step hydrothermal synthesis and photocatalytic performance of $ZnWO_4/Bi_2WO_6$ composite photocatalysts for efficient degradation of acetaldehyde under UV light irradiation

Mirabbos Hojamberdiev[a,*], Ken-ichi Katsumata[a], Koji Morita[b], Sara Aldabe Bilmes[c], Nobuhiro Matsushita[a], Kiyoshi Okada[a]

[a] Materials and Structures Laboratory, Tokyo Institute of Technology, 4259 Nagatsuta, Midori, Yokohama, 226-8503 Kanagawa, Japan
[b] Advanced Materials Processing Unit, Advanced Ceramics Group, National Institute for Materials Science, 1-2-1 Sengen, Tsukuba, 305-0047 Ibaraki, Japan
[c] Instituto de Química Física de los Materiales, Medio Ambiente y Energía (INQUIMAE), Facultad de Ciencias Exactas y Naturales, Universidad de Buenos Aires, Pabellón II, Ciudad Universitaria, C1428EHA-Buenos Aires, Argentina

ARTICLE INFO

Article history:
Received 23 November 2012
Received in revised form 9 February 2013
Accepted 12 March 2013
Available online 18 March 2013

Keywords:
Bismuth tungstate
Composite photocatalyst
Heterostructure
Hydrothermal synthesis
UV light irradiation
Zinc tungstate

ABSTRACT

Bi_2WO_6 with different Bi^{3+} ion concentrations (0–30 mol%) is incorporated with the $ZnWO_4$ photocatalyst to improve the photocatalytic efficiency by forming a $ZnWO_4/Bi_2WO_6$ composite photocatalyst with hierarchical heterostructure via a one-step hydrothermal method. X-ray diffraction and Raman spectroscopy analyses confirm the presence of $ZnWO_4$ and Bi_2WO_6 as main phases in the composite photocatalyst. Scanning electron microscopy and transmission electron microscopy observations reveal that the rice- and plate-like Bi_2WO_6 nanoparticles were either separate or attached to the surface of quasi-spherical $ZnWO_4$ particles. A gradual increase in the Bi_2WO_6 content of the composite photocatalyst results in a monotonic shift of the absorption edge from ca. 355 nm to longer wavelengths up to ca. 450 nm. The photocatalytic performance of the $ZnWO_4/Bi_2WO_6$ composite photocatalyst was evaluated by investigating the degradation of gaseous acetaldehyde (AcH) under UV light irradiation. Only the composite photocatalyst synthesized with 30 mol% Bi^{3+} exhibits higher photocatalytic activity under UV light irradiation compared with both individual $ZnWO_4$ and Bi_2WO_6, and with a mechanically mixed $ZnWO_4/Bi_2WO_6$ composite photocatalyst. The enhanced photocatalytic activity is attributed to the *n-n* isotype junction formed between the two semiconductors and the charge separation of each semiconductor.

1. Introduction

Semiconductors exhibit several properties that are strongly sensitive to their structures, and are considered to be important materials for environmental applications, such as air purification, water disinfection, hazardous waste remediation, and water purification [1,2]. Among them, metal tungstates-based semiconductors have been intensively investigated as potential candidates for photocatalytic processes. As a member of the metal tungstate family, zinc tungstate ($ZnWO_4$) crystallizes in the monoclinic wolframite structure and has a high application potential in various fields as an X-ray, γ-scintillator, microwave system, solid-state laser host, gas and humidity sensors, acoustic and optical fibers, and magnetic material, due to characteristics, such as high chemical stability, high average refractive index, high X-ray absorption coefficient, high light yield, short decay time, and long afterglow to luminescence [3,4]. There have been a number of recent reports concerning improvement of the optical properties of $ZnWO_4$ by the introduction of rare earth ions [5–8]; excitation of the tungstate group may effectively transfer energy to the rare earth element and become potential phosphors.

The molecular and electronic versatility, reactivity, and stability of $ZnWO_4$ have also made it a candidate environmental material for the photodegradation of organic water pollutants and water splitting [9–12]. The difference in the photocatalytic activities of $ZnWO_4$ with different morphologies, including nanorods [9], porous films [11], and nanoparticles [13], is mainly due to differences in crystallinity and specific surface area. Moreover, the photocatalytic activity of $ZnWO_4$ could also be influenced by the crystal growth orientation [14], nanorod aspect ratio [15], OH^- defects [16], ion doping [17–19], and the porous structure [11]. However, $ZnWO_4$ with a wide band gap of 3.75 eV [20] exhibits low photocatalytic activity, but the effective combination of photon absorption, bulk diffusion, and surface transfer of photoinduced charge-carriers could lead to enhancement of its photocatalytic activity.

* Corresponding author. Tel.: +81 45 924 5369; fax: +81 45 924 5358.
E-mail addresses: hmirabbos@gmail.com, mhojamberdiev.m.aa@m.titech.ac.jp, hmirabbos@hotmail.com (M. Hojamberdiev).

0926-860X/$ – see front matter © 2013 Elsevier B.V. All rights reserved.
http://dx.doi.org/10.1016/j.apcata.2013.03.014

Bismuth tungstate (Bi_2WO_6) is one of the simplest members of the Aurivillius oxide family of layered perovskites with the general formula $Bi_2A_{n-1}B_nO_{3n+3}$ (A = Ca, Sr, Ba, Pb, Na, K; B = Ti, Nb, Ta, Mo, W, Fe; and n = number of perovskite-like layers $(A_{n-1}B_nO_{3n+1})^{2-}$), which are structurally composed of alternating perovskite-like and fluorite-like blocks. Bi_2WO_6 exhibits several important physical properties, such as ferroelectric piezoelectricity, pyroelectricity, catalytic behavior, oxide anion conductivity, nonlinear dielectric susceptibility, and luminescence. Bi_2WO_6, which has a band gap of 2.80 eV, has excellent photocatalytic activity for O_2 evolution and for the mineralization of $CHCl_3$ and CH_3CHO into CO_2 under visible light irradiation [21,22].

Recently, composite photocatalysts have received much attention due to enhanced photocatalytic activity that results from the formation of heterojunction structures. The combination of two semiconductors in contact that have different redox energy levels of their corresponding conduction and valence bands can be considered to be one of the most promising methods to improve charge separation, increase the lifetime of charge carriers, and enhance the efficiency of the interfacial charge transfer to the adsorbed substrate [23]. To date, there has been much effort to enhance the photodegradation efficiency of Bi_2WO_6 by coupling with other semiconductors, such as TiO_2 [24], ZnO [25], Bi_2O_3 [26], Co_2O_3 [27], Bi_2S_3 [28], graphene [29], g-C_3N_4 [30], BiOI [31], and $CeVO_4$ [32]. Very recently, the $Bi_2WO_6/ZnWO_4$ composite photocatalyst, which is composed of Bi_2WO_6 nanoparticles grown on primary $ZnWO_4$ nanorods, was obtained by a simple hydrothermal method [33]. Although promising results have been obtained with this composite nanocatalyst, the efficiency is limited due to the rapid recombination of photogenerated charge carriers and the back reaction of intermediate chemical species [34]. Nanostructured powders do not support internal space charges; therefore, the photogenerated electrons and holes are not efficiently separated [35]. Another composite photocatalyst was also synthesized using a two-step hydrothermal method and the photocatalytic activity was evaluated for the degradation of Rhodamine B under UV light irradiation [36].

We propose a one-step strategy for the preparation of the $ZnWO_4/Bi_2WO_6$ composite photocatalyst by hydrothermal processing, and the photocatalytic activity of the resultant composite photocatalyst is evaluated for the degradation of acetaldehyde (AcH) under UV light irradiation. The $ZnWO_4/Bi_2WO_6$ ratio in the composite photocatalyst was also varied to determine the optimal composition of the photocatalyst for higher photocatalytic efficiency under UV light irradiation.

2. Experimental

2.1. Synthesis

The $ZnWO_4/Bi_2WO_6$ composite photocatalyst was prepared using a one-step hydrothermal method. The experimental procedures were as follows: first, 2.5 mmol of $Zn(NO_3)_2{\cdot}6H_2O$ (Wako Pure Chemical Industries, Ltd., Japan) was dissolved in 15 mL of deionized water (Millipore Milli-Q Plus purification system, 18.2 MΩ cm), 2.5 mmol of $Bi(NO_3)_3{\cdot}5H_2O$ (Wako Pure Chemical Industries, Ltd., Japan) was dissolved in 15 mL of diluted nitric acid, and 2.5 mmol of Na_2WO_4 (Wako Pure Chemical Industries, Ltd., Japan) was dissolved in 15 mL of deionized water. 15 mL of bismuth nitrate solution with different mole percentages (0–30 mol%) was introduced into the zinc nitrate solution, and then 15 mL of sodium tungstate solution was added under vigorous stirring. The pH of the suspension was adjusted by the addition of aqueous ammonia (Wako Pure Chemical Industries, Ltd., Japan) to determine the optimal synthesis conditions. After being well homogenized for 30 min, the white-colored suspension obtained was transferred into a 40 mL Teflon-lined stainless steel autoclave. The autoclave was sealed and maintained at 160 °C for 12 h. After hydrothermal treatment, the autoclave was allowed to cool to room temperature. The resulting precipitate was collected by centrifugation, washed with deionized water several times and dried at 80 °C for 8 h.

2.2. Characterization

The crystalline phases formed in the as-synthesized composite photocatalyst samples were identified by X-ray powder diffraction (XRD) using an RINT-2100 diffractometer (Rigaku, Japan) with monochromated Cu Kα radiation (λ = 1.5405 Å) at 40 kV and 40 mA. The XRD patterns of the samples were measured at a scanning rate of 2°/min in the 2θ range of 10–70°. The crystalline phases present in the as-synthesized composite photocatalysts were also confirmed using a T64000 Raman spectroscopy (Horiba Jobin Yvon S.A.S., France) with an Ar laser (514.5 nm) operated at 50 mW. The morphologies and particle sizes of the as-synthesized composite photocatalysts were examined using an S-4500 ultra high resolution scanning electron microscope (SEM) (Hitachi, Japan), operated at an acceleration voltage of 15 kV. The SEM was also equipped with an X-ray energy dispersive spectroscopy (EDS) attachment for elemental analysis. Transmission electron microscopy (TEM) observations were performed on powder samples using a JEM-2010UHR electron microscope (JEOL, Japan), operated at an acceleration voltage of 200 kV to distinguish the crystal structures and particle sizes. For TEM observation, a powder sample was dispersed in ethanol under ultrasonication, and a small amount of the suspension was dropped on the holey carbon grid. UV–vis diffuse reflectance spectra of the composite photocatalysts were recorded at room temperature with a Lambda 950 UV/vis/NIR spectrophotometer (PerkinElmer, USA) in the wavelength range of 200–600 nm, using $BaSO_4$ as a reference.

2.3. Photodegradation experiments

Acetaldehyde (AcH), which is a typical indoor air pollutant, was selected as a probe molecule to evaluate the photocatalytic activity of the as-synthesized composite photocatalyst under UV light irradiation. Photodegradation of AcH was conducted in a batch-type reactor over the as-synthesized composite photocatalyst at room temperature (25 °C). The photocatalyst (50 mg) was placed in the 500 mL Pyrex® glass reaction vessel. Pure air (Taiyo Nippon Sanso Corp., Japan) was blown through the reaction vessel at room temperature to remove any air contaminants. A certain amount of AcH was then introduced into the reaction vessel using a 2 mL Pressure-Lok® glass syringe until the concentration of AcH in the reactor reached ca. 250 ppm. After equilibration of adsorption onto the composite photocatalyst in the dark for 24 h, the reactor was placed under an FL10BLB black-light lamps (Toshiba, Japan) with a wavelength range of 290–420 nm with a peak at 352 nm. UV light was emitted with an irradiance of ca. 0.4 mW/cm^2, which was measured with a UV 340 UV light meter (Lutron Electronic Enterprise Co., Ltd., Taiwan). The decrease and increase in the respective concentrations of AcH and CO_2 were monitored using a GC-2014 gas chromatograph (Shimadzu, Japan) equipped with a 2 m Porapak-Q column, methanizer and a flame ionization detector, with N_2 employed as the carrier gas.

3. Results and discussion

3.1. Effect of the pH of synthesis solution

The hydrothermal method is mainly based on low-temperature solution processes where the pH of the synthesis solution (or

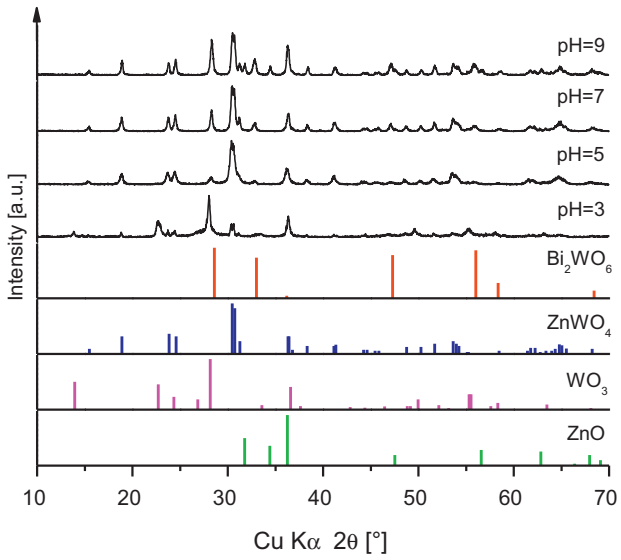

Fig. 1. XRD patterns of $ZnWO_4/Bi_2WO_6$ composite photocatalyst hydrothermally synthesized with 10 mol% Bi^{3+} at 160 °C for 12 h with various pH of synthesizing suspensions.

suspension) is one of the key factors that influences the precipitation of a desired phase. Therefore, preliminary experiments were first performed with various hydrothermal conditions (different pH) for synthesis of the $ZnWO_4/Bi_2WO_6$ composite photocatalyst.

The effect of the synthesis solution pH on the formation of the $ZnWO_4/Bi_2WO_6$ composite photocatalyst was studied using XRD. Fig. 1 shows the XRD patterns of powders hydrothermally synthesized at 160 °C for 12 h with 10 mol% Bi^{3+} at pH 3–9. When the pH of the synthesis suspension was adjusted to 3, the as-synthesized powders predominantly consisted of two crystalline phases: $ZnWO_4$ (JCPDS card no. 15-0774) with the monoclinic wolframite structure and WO_3 (JCPDS card no. 33-1387) with the hexagonal structure, which is an undesirable phase in the composite photocatalyst. As the pH of synthesis suspension was increased to 5, the WO_3 phase completely disappeared, while the orthorhombic Bi_2WO_6 (JCPDS card no. 39-0256) phase began to form, which indicated that a synthesis suspension pH of 3 was more favorable for the formation of the WO_3 phase rather than the Bi_2WO_6 phase. All reflections in the XRD pattern of the powders that were hydrothermally synthesized at pH 7 could be readily assigned to the $ZnWO_4$ and Bi_2WO_6 phases. No XRD reflections corresponding to impurity phases were detected in these composite photocatalysts. Further increase in the pH of the synthesis suspension to 9 led to the simultaneous precipitation of $ZnWO_4$ and Bi_2WO_6 as major phases, with the inclusion of another undesired phase, ZnO (JCPDS card no. 65-3411). Comparison of all the XRD data for the products hydrothermally synthesized at different pH indicated that the only pH 7 was favorable for the formation of both the $ZnWO_4$ and Bi_2WO_6 phases without any impurity phases under the current experimental conditions.

Fig. 2 shows the microstructural features of powders hydrothermally synthesized at 160 °C for 12 h with 10 mol% Bi^{3+} at pH 3–9. The powders hydrothermally synthesized at pH 3 have large irregular particles mixed with submicron rod- and plate-like particles. EDS results (not shown here) suggest that the large irregular particles are $ZnWO_4$, whereas the rod- and plate-like particles are representative of the WO_3 phase. The powders hydrothermally synthesized at pH 5 are mostly agglomerated quasi-spheres constructed from the aggregation of $ZnWO_4$ nanorods. A few plate-like particles are also visible, which indicates the presence of the Bi_2WO_6 phase. These results are consistent with the XRD data shown in Fig. 1. Hydrothermal synthesis at pH 7 has a pronounced effect on the morphology of the resultant powders; the majority of particles shown in Fig. 2 are submicron-sized $ZnWO_4$ rod-like

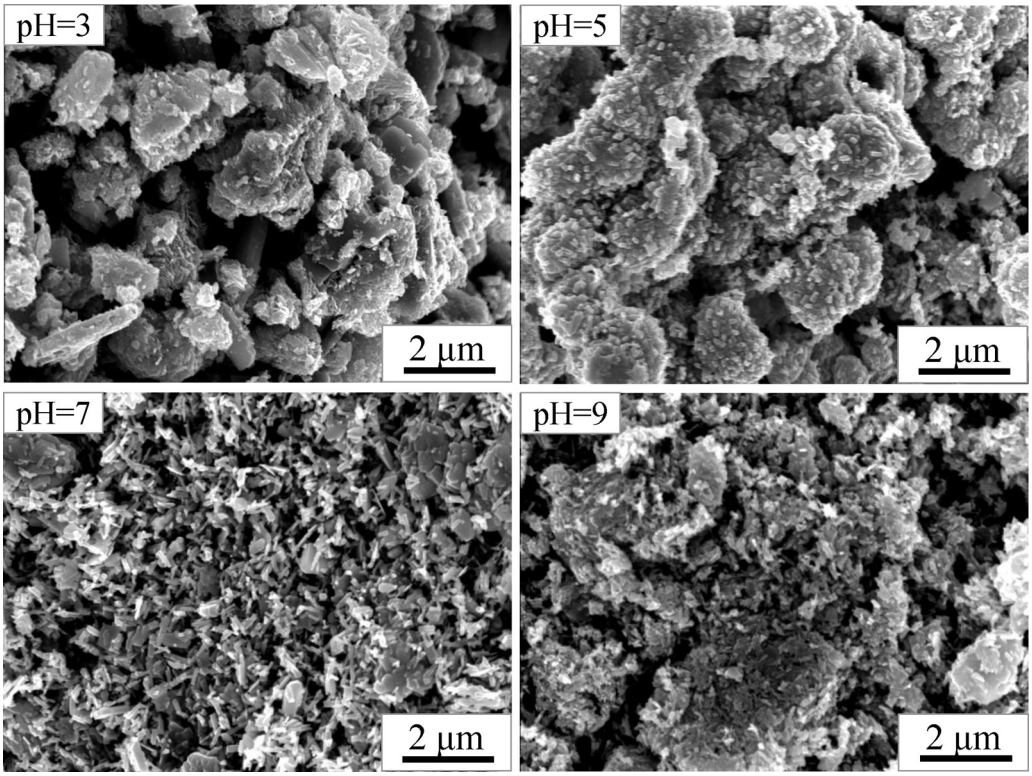

Fig. 2. SEM micrographs of $ZnWO_4/Bi_2WO_6$ composite photocatalyst hydrothermally synthesized with 10 mol% Bi^{3+} at 160 °C for 12 h with various pH of synthesizing suspensions.

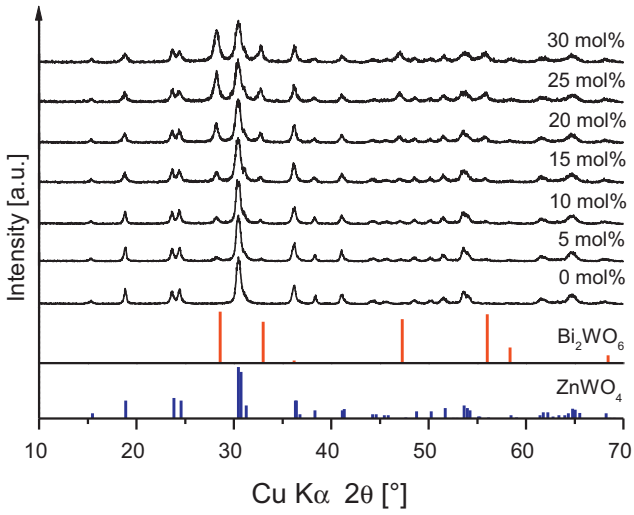

Fig. 3. XRD patterns of $ZnWO_4/Bi_2WO_6$ composite photocatalyst hydrothermally synthesized at 160 °C for 12 h with various Bi^{3+} ion concentrations at pH 7.

particles, and the number of plate-like Bi_2WO_6 particles has also increased with the increase in the pH. With further increase of the synthesis suspension pH to 9, the sizes of the rod- and plate-like particles are decreased, along with the formation of small irregular particles of ZnO. The SEM results demonstrate that the morphology of the composite photocatalyst can easily be tailored by adjustment of the pH. We have also investigated the effect of the synthesis suspension pH on the morphologies of $ZnWO_4$ [37], YVO_4:Eu^{3+} [38,39], and PbI_2 [40] under hydrothermal conditions.

3.2. Effect of Bi^{3+} ion concentration

The Bi^{3+} ion concentration was varied from 0 to 30 mol% in the synthesis suspension to obtain various mole fractions of Bi_2WO_6 in the composite photocatalyst and investigate the contribution of Bi_2WO_6 to the degradation of AcH under UV light irradiation. Fig. 3 shows the XRD patterns of composite photocatalyst hydrothermally synthesized at 160 °C for 12 h with various Bi^{3+} ion concentrations at pH 7. As expected, the sample hydrothermally synthesized without Bi^{3+} ions contains only the $ZnWO_4$ phase. In contrast, the introduction of 5–30 mol% Bi^{3+} into the synthesis suspension resulted in composite photocatalysts composed of both the $ZnWO_4$ and Bi_2WO_6 phases. No XRD reflections belonging to secondary phases were evident, even in the composite photocatalyst synthesized with the highest Bi^{3+} ion concentration (30 mol%). The intensity of the reflections corresponding to the Bi_2WO_6 phase gradually increased with the Bi^{3+} ion concentration. It should be noted that no peak shift was observed in the XRD patterns for both phases, which provides evidence that the current experimental conditions were not adequate for an ion doping process. This was also confirmed by comparison of the calculated lattice parameters for the phases present in the samples. Furthermore, the $ZnWO_4$ and Bi_2WO_6 phases in the composite photocatalyst were quantitatively analyzed by the Rietveld method using the obtained XRD patterns. The percentage of Bi_2WO_6 phase in the composite photocatalyst increases with the increase in the Bi^{3+} ion concentration as follows: 0% (0 mol%) < 6% (5 mol%) < 9% (10 mol%) < 12% (15 mol%) < 22% (20 mol%) < 29% (25 mol%) < 34% (30 mol%). The $ZnWO_4$ phase still prevails as the predominant fraction in the composite photocatalyst. Thus, the direct relationship between the Bi^{3+} ion concentration added and the mole fraction of Bi_2WO_6 phase present in the composite photocatalyst was verified.

Fig. 4 shows the SEM micrographs of samples hydrothermally synthesized at 160 °C for 12 h with various Bi^{3+} ion concentrations at pH 7. The pure $ZnWO_4$ powders without Bi^{3+} have larger irregular particles formed by the aggregation of nano- and submicron-sized particles. With the addition of 5 mol% Bi^{3+} to the synthesis system, the $ZnWO_4/Bi_2WO_6$ composite photocatalyst was obtained with irregular morphology, and the particle size was significantly diminished in comparison to that of pure $ZnWO_4$. The morphologies of the $ZnWO_4/Bi_2WO_6$ composite photocatalysts obtained with 10–30 mol% Bi^{3+} shown in Fig. 4 are principally comprised of three types of distinctive particles: large micrometer-sized quasi-spheres, and nanometer-sized rice- and plate-like particles. These particles become larger and more distinct with the increase in Bi^{3+} from 10 to 30 mol%, which suggests that the incorporation of Bi^{3+} ions is essential for alteration of the overall morphology of the composite photocatalyst.

To discriminate the particles and gain insight into the crystal structures, TEM analysis was conducted on the $ZnWO_4/Bi_2WO_6$ composite photocatalyst that was hydrothermally synthesized at 160 °C for 12 h with 30 mol% Bi^{3+} at pH 7. Fig. 5 shows the TEM micrographs (a, c, d), EDS spectra (b), selected area diffraction (SAD) patterns (insets), and HRTEM micrographs (e, f) of the $ZnWO_4/Bi_2WO_6$ composite photocatalyst. The TEM image of the composite photocatalyst in Fig. 5a indicates the coexistence of three different particles in the composite photocatalyst, which is consistent with the SEM observations. Elemental analysis results of these three different particles using EDS are shown in Fig. 5b. The quasi-spherical particles (0.8–1.3 μm) correspond to the $ZnWO_4$ phase and the rice (400–600 nm long and 80–150 nm wide)- and plate (300–500 nm diameter)-like particles to the Bi_2WO_6 phase. Figs. 5c and d show that a number of rice- and plate-like Bi_2WO_6 particles are attached to the surface of the quasi-spherical $ZnWO_4$ particles, and the rice-like Bi_2WO_6 particles are constructed with a significant amount of tiny nanorods. Separately located particles were most probably detached from the composite photocatalyst by strong utrasonication used during the TEM sample preparation. The ring-like SAD patterns shown in the insets of Figs. 5c and d reveal the overall polycrystallinity of the quasi-spherical $ZnWO_4$ particles and the rice-like Bi_2WO_6 particles. The HRTEM images shown in Figs. 5e and f confirm uniform lattice fringes with an interval of 0.362 nm that correspond to the d spacing between adjacent (110) crystallographic planes of monoclinic $ZnWO_4$, while the lattice fringes of $d = 0.320$ are consistent with the (131) crystallographic planes of orthorhombic Bi_2WO_6. The SEM and TEM observations indicate that the as-synthesized composite photocatalyst has a contacting junction structure between $ZnWO_4$ and Bi_2WO_6 crystals.

Although time-dependent experiments were not performed in this study, based on previous reports, we briefly present the formation processes for the $ZnWO_4/Bi_2WO_6$ composite photocatalyst, without a strong intention to provide an exact mechanism. It is supposed that in the competitive precipitation process, the formation of tiny crystalline nuclei of $ZnWO_4$ in the supersaturated medium occurs first. While the crystal growth process of $ZnWO_4$ probably occurs at the expense of smaller crystals, according to the Gibbs-Thompson theory, tiny crystalline nuclei of Bi_2WO_6 begin to form from Bi^{3+} and remaining $[WO_4]^{2-}$ ions. Under hydrothermal treatment, $ZnWO_4$ and Bi_2WO_6 nanorods form from tiny nuclei, due to their anisotropic nature, and are further self-assembled into quasi-spheres and rice- and plate-like particles, respectively, by an oriented attachment process, of which the driving force is a reduction of the surface energy of crystal planes [41,42]. Consequently, a number of rice- and plate-like particles of Bi_2WO_6 are attached to the surface of quasi-spherical particles of $ZnWO_4$, where a moderate junction structure is formed.

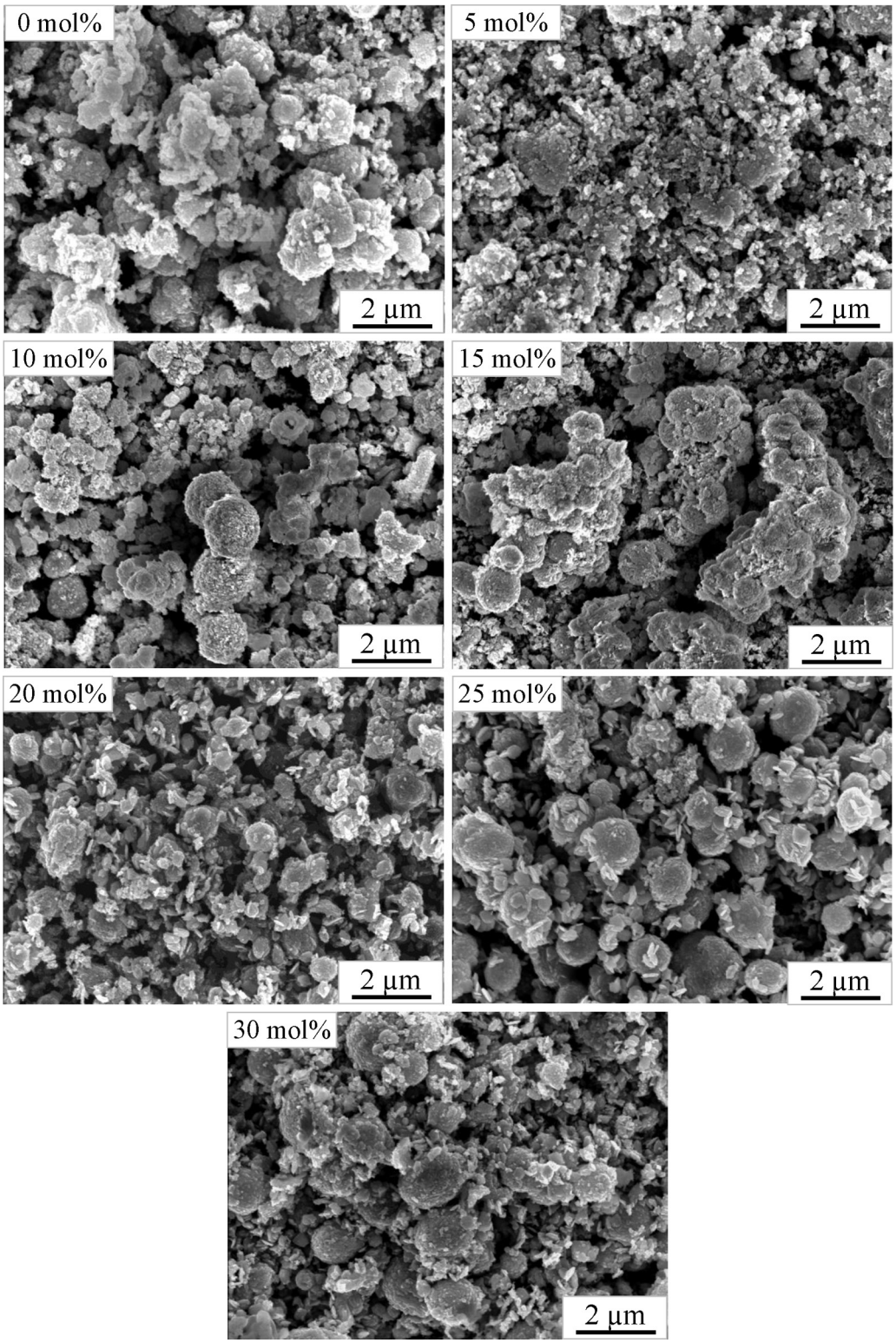

Fig. 4. SEM micrographs of $ZnWO_4/Bi_2WO_6$ composite photocatalyst hydrothermally synthesized at 160 °C for 12 h with various Bi^{3+} ion concentrations at pH 7.

3.3. Raman spectra

Fig. 6 shows the Raman spectra of $ZnWO_4/Bi_2WO_6$ composite photocatalysts hydrothermally synthesized at 160 °C for 12 h with various Bi^{3+} ion concentrations at pH 7, including that for pure Bi_2WO_6. The space groups of $ZnWO_4$ and Bi_2WO_6 are $P2/c = C_{2h}^4$ and $Pca2_1 = C_{2v}^5$, respectively. Group theory analysis for wolframite-type $ZnWO_4$ predicts 36 lattice modes, of which 18 even vibrations ($8A_g + 10B_g$) are Raman active [43]. The Raman peaks at ca. 126, 148, 166, 191, 198, 270, 277, 316, 343, 356, 408, 516, 550, 680, 710 and 787 cm^{-1} are assignable to the internal vibrations of the WO_6 octahedra of $ZnWO_4$. Note that two Raman peaks at 93 and 908 cm^{-1} are not shown here. The Raman spectrum of pure Bi_2WO_6 with the orthorhombic *Pbca(61)* space group shown in Fig. 6 is similar to that of the orthorhombic $Pca2_1$ space group [44]; therefore, it is considered that the Raman

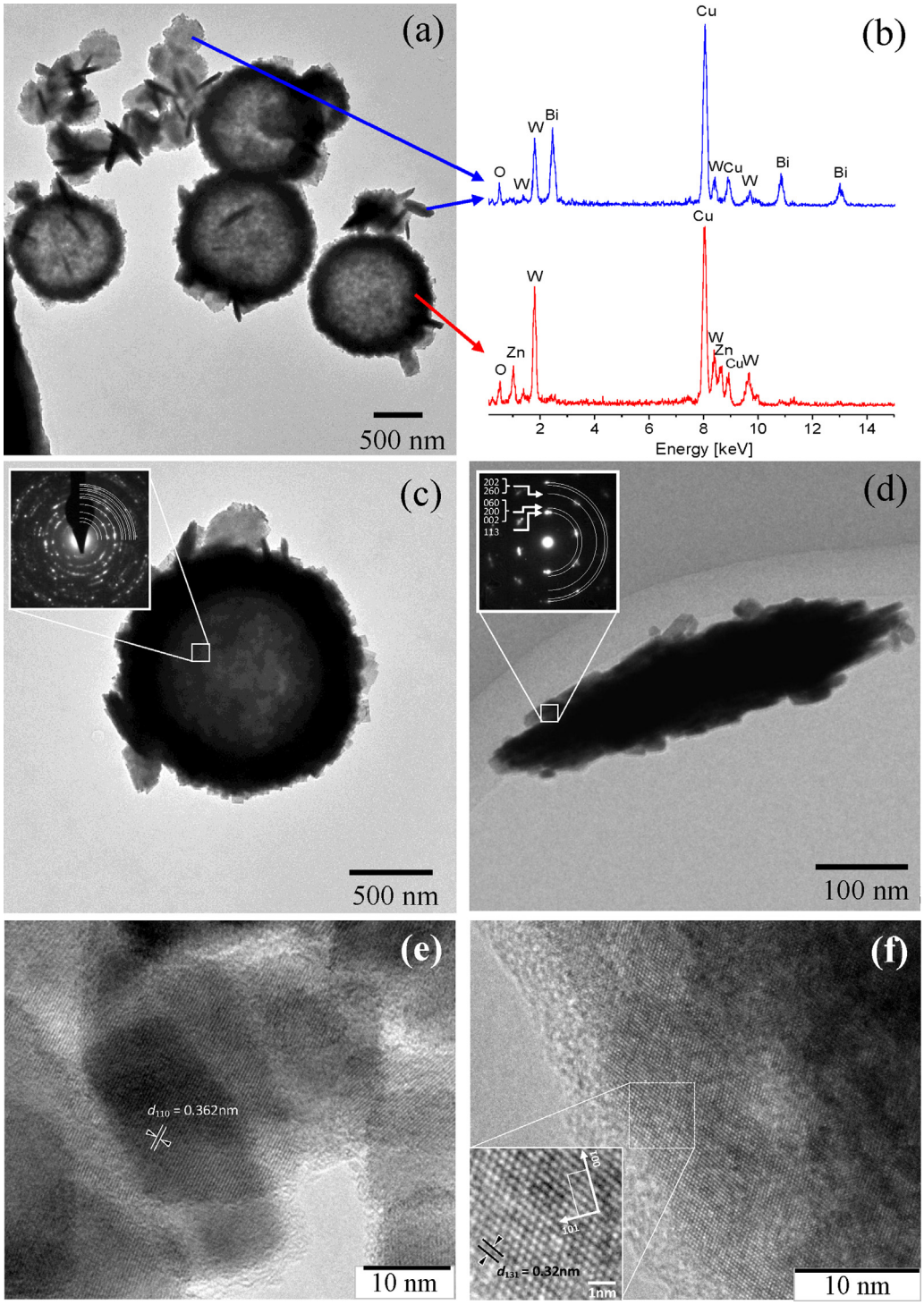

Fig. 5. TEM micrographs (a, c, d), EDS spectra (b), SAD patterns (insets), and HRTEM micrographs (e, f) of $ZnWO_4/Bi_2WO_6$ composite photocatalyst hydrothermally synthesized at 160 °C for 12 h with 30 mol% Bi^{3+} at pH 7.

peaks of the *Pbca(61)* phase can be assigned to those modes of the *Pca2₁* phase. The number of optic modes for the *Pca2₁* phase is $26A_1 + 27A_2 + 26B_1 + 26B_2$. The A_2 modes are Raman active and the A_1, B_1, and B_2 modes are both IR and Raman active [45]. From the Raman spectra of composite photocatalyst and Bi_2WO_6, the Raman peaks at 788 and 703 cm^{-1} can be assigned to the symmetric and asymmetric stretching modes of WO_6 octahedra that involve motions of the apical and equatorial oxygen atoms perpendicular to and within layers, respectively. The Raman peaks at 412, 300, 278, 256, 215 and 187 cm^{-1} can be attributed to the bending modes of WO_6 octahedra and the stretching and bending modes of BiO_6 polyhedra. The Raman peaks at 140 and 147 cm^{-1} may be assigned to the translations of tungsten and bismuth ions [44].

As the Bi^{3+} ion concentration in the synthesis suspension increases, the intensity of the Raman modes corresponding to the monoclinic $ZnWO_4$ phase is decreased. In addition, all the Raman spectra we carefully examined and no considerable shift of the Raman peaks of the $ZnWO_4$ and Bi_2WO_6 phases was confirmed. The overall intensities of the Raman spectra for the composite

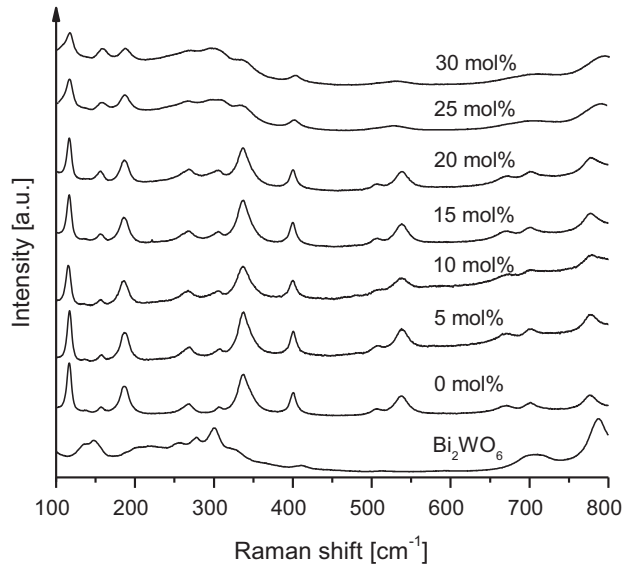

Fig. 6. Raman spectra of $ZnWO_4/Bi_2WO_6$ composite photocatalyst hydrothermally synthesized at 160 °C for 12 h with various Bi^{3+} ion concentrations at pH 7.

photocatalysts were significantly enhanced. The enhancement in the intensities of the Raman spectra was primarily postulated by Chen et al. [46] on the basis of two theories: electromagnetic, which relies upon the excitation of localized surface plasmons, and chemical, which rationalizes the effect through the formation of charge-transfer complexes.

3.4. UV–vis diffuse reflectance spectra

Fig. 7 shows the UV–visible diffuse reflectance spectra of $ZnWO_4/Bi_2WO_6$ composite photocatalysts hydrothermally synthesized at 160 °C for 12 h with various Bi^{3+} ion concentrations at pH 7. The light absorbance of pure $ZnWO_4$ lies in the UV region with an absorption edge of ca. 355 nm, and the band gap is estimated to be ca. 3.8 eV. With the introduction of Bi^{3+} ions in the synthesis suspension, $ZnWO_4$ becomes associated with Bi_2WO_6 in the composite photocatalyst. Therefore, compared with pure $ZnWO_4$, a gradual

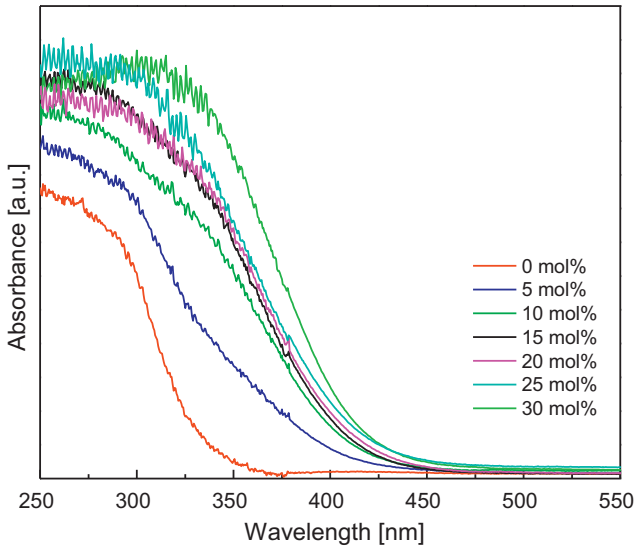

Fig. 7. UV–vis diffuse reflectance spectra of $ZnWO_4/Bi_2WO_6$ composite photocatalyst hydrothermally synthesized at 160 °C for 12 h with various Bi^{3+} ion concentrations at pH 7.

increase in the Bi_2WO_6 content in the composite photocatalyst results in a monotonic shift of the absorption edge from ca. 355 nm to longer wavelengths up to ca. 450 nm, due to the intrinsic transitions of both semiconductors. This also supports the formation of a junction structure between $ZnWO_4$ and Bi_2WO_6 in the composite photocatalyst. The band gaps of the $ZnWO_4/Bi_2WO_6$ composite photocatalysts range from ca. 3.08 to ca. 2.90 eV, in accordance with the Bi_2WO_6 content. Therefore, considering the absorption edge of the composite photocatalyst, it seems reasonable that the as-synthesized composite photocatalyst can be excited under UV light irradiation, which would result in higher photocatalytic activity.

3.5. Photocatalytic activity

The photocatalytic activity of the as-synthesized composite photocatalysts for the photodegradation of AcH under UV light irradiation was evaluated and compared with pure $ZnWO_4$, Bi_2WO_6, and a mechanical mixture of $ZnWO_4/Bi_2WO_6$. AcH is known as a key indoor air pollutant and is also largely formed as an intermediate during the photocatalytic oxidation of other organic compounds [47]. The generation of CO_2 from the photocatalytic oxidation of AcH occurs according to the following reaction:

$$2CH_3CHO + 5O_2 \xrightarrow[h\nu]{\text{photocatalyst}} 4CO_2 + 4H_2O. \quad (1)$$

Fig. 8 shows the photodegradation of AcH over various samples as a function of time, in which C_0 and C are the concentrations of AcH after 24 h adsorption equilibrium in the dark at time t_0 and after a period of UV light irradiation t, respectively. A blank test with 250 ppm AcH in the absence of a photocatalyst was also run under UV light irradiation, where the concentration of AcH decreases negligibly over time, which indicates the stability of AcH under UV light irradiation. The same experimental conditions were applied for all samples. The incorporation of Bi_2WO_6 in $ZnWO_4$ was observed to enhance the photocatalytic activity compared to that of pure $ZnWO_4$. Nevertheless, only the composite photocatalyst with 30 mol% Bi^{3+} exhibited complete conversion (100%) of AcH into CO_2 after 6 h of UV light irradiation, whereas the mechanically mixed counterpart ($ZnWO_4$/30 mol% Bi_2WO_6 composite photocatalyst) had a slightly lower conversion (94%) of AcH into CO_2.

Mechanical mixing tends to cause the formation of crystal lattice defects that serve as electron-hole recombination centers for the composite photocatalyst. However, it is expected that a one-step synthesis of the composite photocatalyst would enable better contact between the two semiconductors, which would facilitate charge transfer from one particle to another. The overall conversion of AcH into CO_2 for the as-synthesized samples was calculated using the formula:

$$\text{Conversion } (\%) = \left(\frac{[CO_2]}{2[CH_3CHO]}\right) \times 100 \quad (2)$$

The following results were obtained: 36.2% ($ZnWO_4$) < 44.0% (Bi_2WO_6) < 52.8% (5 mol%) < 60.8% (10 mol%) < 71.2% (15 mol%) < 79.8% (20 mol%) < 86.2% (25 mol%) < 94.0% (mechanical mixture of $ZnWO_4$/30 mol% Bi_2WO_6) < 100% (30 mol%). In addition, apparent first-order rate constants (k) for the degradation of AcH were calculated using the Langmuir-Hinshelwood kinetic model:

$$-ln\left(\frac{C}{C_0}\right) = kt, \quad (3)$$

where C_0 and C are the concentrations of AcH after 24 h adsorption equilibrium in the dark at time t_0 and after a period of UV light irradiation t, respectively. A good linear relationship was observed for the $\ln(C/C_0)$ vs. time (t) plot over the first 4 h; therefore, the apparent rate constant (k) was calculated by fitting this portion of the linear plot. The calculated

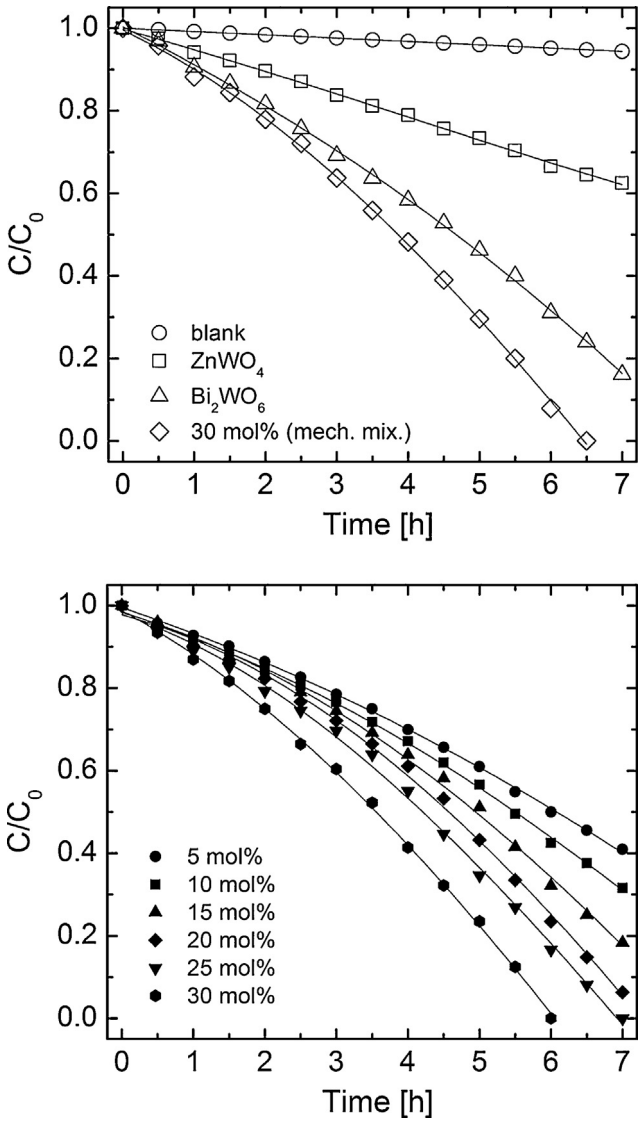

Fig. 8. Photocatalytic oxidative decomposition of AcH (250 ppm) without a photocatalyst (blank), over $ZnWO_4$, Bi_2WO_6, a mechanicall mixture of $ZnWO_4/Bi_2WO_6$ (30 mol%), and over the as-synthesized $ZnWO_4/Bi_2WO_6$ composite photocatalyst samples (50 mg) under UV light irradiation (ca. 0.4 mW/cm^2). C_0 and C are the concentrations of AcH at time t_0 and t, respectively.

apparent rate constant increases in the following order: 0.0583 min^{-1} ($ZnWO_4$) < 0.0820 min^{-1} (5 mol%) < 0.0930 min^{-1} (10 mol%) < 0.1030 min^{-1} (15 mol%) < 0.1132 min^{-1} (20 mol%) < 0.1230 min^{-1} (Bi_2WO_6) < 0.1298 min^{-1} (25 mol%) < 0.1573 min^{-1} (mechanical mixture of $ZnWO_4$/30 mol% Bi_2WO_6) < 0.1840 min^{-1} (30 mol%). The apparent rate constant increases with the Bi_2WO_6 content in the composite photocatalyst. The highest apparent rate constant was observed for the sample synthesized with 30 mol% Bi^{3+}, which is attributed to successful charge transfer achieved from one semiconductor to another. Compared with the previously reported results for the same composite system prepared by a simple hydrothermal method [33], the addition of 30 mol% Bi^{3+} was much higher, and the photocatalytic activity was monotonically increased with the Bi_2WO_6 content. The main reason for this difference may be related to the partial coverage of the surface of the quasi-spherical $ZnWO_4$ particles, as shown in Fig. 5, which allows light absorption to occur in the $ZnWO_4$ particles. It has been widely reported that if a core particle is thickly covered by a shell, then interfacial transfer may be impeded or no light absorption in the core may occur, which would lead to lower photocatalytic activity [34,48].

It is evident that an increase in the Bi_2WO_6 content leads to higher photocatalytic activity of the composite photocatalyst, even though some of the Bi_2WO_6 particles are not attached to the surface of the quasi-spherical $ZnWO_4$ particles. This is because the layered structure of Bi_2WO_6 is favorable for charge transfer, which retards the recombination of photogenerated holes and electrons [49,50], and the higher specific surface area also provides more active reaction sites for the photocatalytic reaction to occur on the surface of the photocatalyst [51]. In addition, the valence band of the Bi_2WO_6 photocatalyst consists of O 2*p* and Bi 6*p* hybrid orbitals, and the bottom of the conduction band is formed by the W 5*d* orbitals with a small contribution from the Bi 6*p* orbitals. The hybridization of the Bi 6*s* and O 2*p* levels also causes the valence band to become largely dispersed, which favors the mobility of photoinduced holes in the valence band, which is beneficial for photocatalytic oxidation reactions [52].

To clearly explain the enhancement in the photocatalytic activity of the $ZnWO_4/Bi_2WO_6$ composite photocatalysts in terms of *n*-*n* isotype junctions, further investigation is required. $ZnWO_4$ and Bi_2WO_6 are *n*-type semiconductors; therefore, it is supposed that during UV light irradiation of the *n*-*n* isotype junction, the electrons from the $ZnWO_4$ region diffuse into the Bi_2WO_6 region, which creates an accumulation of negative charges in the Bi_2WO_6 region and an accumulation of positive charges in the $ZnWO_4$ region in the vicinity of the junction. This is expected to provide an internal electrostatic field directed from the $ZnWO_4$ region to the Bi_2WO_6 region, which creates an energy barrier for the electron transfer from $ZnWO_4$ to Bi_2WO_6 [53,54]. Moreover, another mechanism may be attributed to the state of tungsten present in both semiconductors. W^{6+} is generally a strong oxidizing agent that is readily reduced to W^{5+}. The band structure diagram presented in Ref. [55] features a donor level that arises from the $5d^1$ configuration of W^{5+}, between the valence (O^{2-}) and conduction (W^{6+}) bands. Therefore, it is considered that both W^{6+} and W^{5+} are present in the composite photocatalyst synthesized in this study. Thus, by reaching a saturation level of W^{6+}-to-W^{5+} conversion, the presence of oxygen can further re-oxidize W^{5+} to W^{6+} [56], which could also contribute to the photocatalytic enhancement of the composite photocatalyst.

4. Conclusions

The effect of Bi_2WO_6 content in the $ZnWO_4/Bi_2WO_6$ composite photocatalyst on the performance for the photocatalytic degradation of AcH under UV light irradiation was investigated in this study. A gradual increase in the Bi_2WO_6 content of the composite photocatalyst resulted in a monotonic shift of the absorption edge from ca. 355 nm to longer wavelengths up to ca. 450 nm. The composite photocatalyst synthesized with 30 mol% Bi^{3+} exhibited higher photocatalytic activity for the conversion of AcH into CO_2 under UV light irradiation compared with that for individual $ZnWO_4$ and Bi_2WO_6, and that for a mechanically mixed $ZnWO_4/Bi_2WO_6$ composite photocatalyst. The enhancement of the photocatalytic activity can be attributed to *n*-*n* isotype junctions formed between the two semiconductors and to the charge separation of each semiconductor, because the $ZnWO_4$ and Bi_2WO_6 particles in the composite photocatalyst are either joined or separate.

Acknowledgements

MH would like to thank the Japan Society for the Promotion of Science (JSPS) for the postdoctoral fellowship under which the present study was carried out. The authors wish to thank

Mr. Jean-Christophe Jaud and Mr. Yukihiro Komatsubara for performing the Rietveld analysis and TEM measurements, respectively.

References

[1] M.R. Hoffmann, S.T. Martin, W. Choi, D.W. Bahneman, Chem. Rev. 95 (1995) 69–96.
[2] A. Fujishima, T.N. Rao, D.A. Tryk, J. Photochem. Photobiol. C 1 (2000) 1–21.
[3] T. Oi, K. Takagi, T. Fukazawa, Appl. Phys. Lett. 36 (1980) 278–279.
[4] P.J. Born, D.S. Robertson, P.W. Smith, G. Hames, J. Reed, J. Telfor, J. Lumin. 24–25 (1981) 131–134.
[5] F.-S. Wen, X. Zhao, H. Huo, J.-S. Chen, E. Shu-Lin, J.-H. Zhang, Mater. Lett. 55 (2002) 152–157.
[6] F. Yang, C. Tu, J. Li, G. Jia, H. Wang, Y. Wei, Z. You, Z. Zhu, Y. Wang, X. Lu, J. Lumin. 126 (2007) 623–628.
[7] H.Y. He, Phys. Status Solidi B 246 (2009) 177–182.
[8] F. Yang, C. Tu, H. Wang, Y. Wei, Z. You, G. Jia, J. Li, Z. Zhu, X. Lu, Y. Wang, Opt. Mater. 29 (2007) 1861–1865.
[9] H. Fu, J. Lin, L. Zhang, Y. Zhu, Appl. Catal. A 306 (2006) 58–67.
[10] X. Zhao, Y. Zhu, Environ. Sci. Technol. 40 (2006) 3367–3372.
[11] X. Zhao, W. Yao, Y. Wu, S. Zhang, H. Yang, Y. Zhu, J. Solid State Chem. 179 (2006) 2562–2570.
[12] M. Hojamberdiev, G. Zhu, Y. Xu, Mater. Res. Bull. 45 (2010) 1934–1940.
[13] G. Huang, C. Zhang, Y. Zhu, J. Alloys Compd. 432 (2007) 269–276.
[14] R. Shi, Y. Wang, D. Li, J. Xu, Y. Zhu, Appl. Catal. B 100 (2010) 173–178.
[15] D. Li, R. Shi, C. Pan, Y. Zhu, H. Zhao, CrystEngComm 13 (2011) 4695–4700.
[16] J. Lin, J. Lin, Y. Zhu, Inorg. Chem. 46 (2007) 8372–8378.
[17] G. Huang, Y. Zhu, J. Phys. Chem. C 111 (2007) 11952–11958.
[18] G. Huang, S. Zhang, T. Xu, Y. Zhu, Environ. Sci. Technol. 42 (2008) 8516–8521.
[19] X.C. Song, Y.F. Zheng, E. Yang, G. Liu, Y. Zhang, H.F. Chen, Y.Y. Zhang, J. Hazard. Mater. 179 (2010) 1122–1127.
[20] M. Bonanni, L. Spanhel, M. Lerch, E. Füglein, G. Müller, F. Jermann, Chem. Mater. 10 (1998) 304–310.
[21] A. Kudo, S. Hijii, Chem. Lett. 28 (1999) 1103–1104.
[22] J. Tang, Z. Zou, J. Ye, Catal. Lett. 92 (2004) 53–56.
[23] Y. Bessekhouad, D. Robert, J.V. Weber, J. Photochem. Photobiol. A 163 (2004) 569–580.
[24] M. Shang, W. Wang, L. Zhang, S. Sun, L. Wang, L. Zhou, J. Phys. Chem. C 113 (2009) 14727–14731.
[25] C.-L. Yu, K. Yang, J.C. Yu, F.-F. Cao, X. Li, X.-C. Zhou, J. Inorg. Mater. 26 (2011) 1157–1163.
[26] M. Ge, Y. Li, L. Liu, Z. Zhou, W. Chen, J. Phys. Chem. C 115 (2011) 5220–5225.
[27] Q. Xiao, J. Zhang, C. Xiao, X. Tan, Catal. Commun. 9 (2008) 1247–1253.
[28] Z. Zhang, W. Wang, L. Wang, S. Sun, ACS Appl. Mater. Interfaces 4 (2012) 593–597.
[29] E. Gao, W. Wang, M. Shang, J. Xu, Phys. Chem. Chem. Phys. 13 (2011) 2887–2893.
[30] L. Ge, C. Han, J. Liu, Appl. Catal. B 108–109 (2011) 100–107.
[31] M. Hojamberdiev, K. Katsumata, N. Matsushita, K. Okada, unpublished results.
[32] M. Hojamberdiev, K. Katsumata, N. Matsushita, K. Okada, unpublished results.
[33] D. He, L. Wang, D. Xu, J. Zhai, D. Wang, T. Xie, ACS Appl. Mater. Interfaces 3 (2011) 3167–3171.
[34] K. Domen, Characterization of photoexcitation processes on solid surfaces, in: M. Anpo (Ed.), Surface Photochemistry, J. Wiley & Sons, Chichester, 1996, pp. 1–18.
[35] W.J. Albery, P.N. Bartlett, J. Electrochem. Soc. 131 (1984) 315–325.
[36] X. Yan, T. Ohno, K. Nishijima, R. Abe, B. Ohtani, Chem. Phys. Lett. 429 (2006) 606–610.
[37] M. Hojamberdiev, G. Zhu, Y. Xu, Mater. Res. Bull. 45 (2010) 1934–1940.
[38] J. Wang, M. Hojamberdiev, Y. Xu, J. Peng, Mater. Chem. Phys. 25 (2010) 82–86.
[39] J. Wang, Y. Xu, M. Hojamberdiev, J. Peng, G. Zhu, Mater. Sci. Eng. B 156 (2009) 42–47.
[40] G. Zhu, M. Hojamberdiev, P. Liu, J. Peng, J. Zhou, X. Bian, X. Huang, Mater. Chem. Phys. 131 (2011) 64–71.
[41] C. Pacholski, A. Kornowski, H. Weller, Angew. Chem. Int. Ed. 41 (2002) 1188–1191.
[42] E.J.H. Lee, C. Ribeiro, E. Longo, E.R. Leite, J. Phys. Chem. B 109 (2005) 20842–20846.
[43] D. Errandonea, F.J. Manjón, N. Garro, P. Rodríguez-Hernández, S. Radescu, A. Mujica, A. Muñoz, C.Y. Tu, Phys. Rev. B 78 (2008) 054116.
[44] M. Maczka, W. Paraguassu, A.G. Souza Filho, P.T.C. Freire, J. Mendes Filho, J. Hanuza, Phys. Rev. B 77 (2008) 094137.
[45] M. Maczka, J. Hanuza, W. Paraguassu, A.G. Souza Filho, P.T.C. Freire, J. Mendes Filho, Appl. Phys. Lett. 92 (2008) 112911.
[46] C. Chen, Y. Zheng, Y. Zhan, X. Lin, Q. Zheng, K. Wei, Dalton Trans. 40 (2011) 9566–9570.
[47] J. Tang, Z. Zou, J. Ye, Angew. Chem. Int. Ed. 43 (2004) 4463–4466.
[48] L. Li, G.S. Rohrer, P.A. Salvador, J. Am. Ceram. Soc. 95 (2012) 1414–1420.
[49] J.-Y. Kim, I. Chung, J.-H. Choy, G.-S. Park, Chem. Mater. 13 (2001) 2759–2761.
[50] Y. Tsunoda, W. Sugimoto, Y. Sugahara, Chem. Mater. 15 (2003) 632–635.
[51] F. Amano, K. Nogami, M. Tanaka, B. Ohtani, Langmuir 26 (2010) 7174–7180.
[52] M. Oshikiri, M. Boero, J. Ye, Z. Zou, G. Kido, J. Chem. Phys. 117 (2002) 7313–7318.
[53] S. Liu, J. Wu, X. Liu, R. Jiang, J. Mol. Catal. A 332 (2010) 84–92.
[54] R.A. Smith, Semiconductors, Second edition, Cambridge University Press, London, 1978.
[55] D.E. Macphee, D. Rosenberg, M.G. Skellern, R.P. Wells, J.A. Duffy, K.S. Killham, J. Solid State Electrochem. 15 (2011) 99–103.
[56] K.K. Akurati, A. Vital, J.-P. Dellemann, K. Michalow, T. Graule, D. Ferri, A. Baiker, Appl. Catal. B 79 (2008) 53–62.